Recent development of Monte Carlo shell model and its application to no-core calculations

T Abe[1], P Maris[2], T Otsuka[1,3,4], N Shimizu[3], Y Tsunoda[1], Y Utsuno[5], J P Vary[2] and T Yoshida[3]

[1] Department of Physics, the University of Tokyo, Hongo, Tokyo 113-0033, Japan
[2] Department of Physics and Astronomy, Iowa State University, Ames, Iowa 50011, USA
[3] Center for Nuclear Study, the University of Tokyo, Hongo, Tokyo 113-0033, Japan
[4] National Superconducting Cyclotron Laboratory, Michigan State University, East Lansing, Michigan 48824, USA
[5] Advanced Science Research Center, Japan Atomic Energy Agency, Tokai, Ibaraki 319-1195, Japan

E-mail: tabe@nt.phys.s.u-tokyo.ac.jp

Abstract. One of the major challenges in nuclear theory is to reproduce and to predict nuclear structure from *ab initio* calculations with realistic nuclear forces. As the current limitation of direct diagonalization of Hamiltonian matrices by Lanczos iteration method is around the order of matrix dimensionality 10^{10} in shell-model calculations, it is difficult to access heavier nuclei beyond the p shell with sufficiently large basis spaces. It is possible to overcome this difficulty by utilizing efficient approximate methods to reproduce full *ab initio* solutions with good precision and quantified uncertainties. Following the major success of the Monte Carlo shell model (MCSM) with an assumed inert core in the *sd*- and pf-shell regions and also by recent developments in the MCSM algorithm, the no-core MCSM is expected to be one of the most powerful tools to meet these conditions. We have performed benchmark calculations in the p-shell region. Results of energies are compared with those in the full configuration interaction and no-core full configuration methods. These are found to be consistent with each other within quoted uncertainties when they could be quantified. We also compare and discuss the radial density of the helium-4 ground state extracted from the MCSM and FCI many-body wave functions.

1. Introduction

One of the major challenges in nuclear physics is to understand nuclear structure and reactions from *ab initio* calculations with realistic nuclear forces. Such calculations have recently become feasible for nuclear many-body systems beyond $A = 4$ due to the rapid evolution of computational technologies. Together with the Green's Function Monte Carlo [1] and Coupled Cluster theory [2], the No-Core Shell Model (NCSM) is one of the relevant *ab initio* methods and has been emerging for about a decade. It is now available for the study of nuclear structure and reactions in the p-shell nuclei [3].

As the NCSM treats all the nucleons democratically, computational demands for the calculations explode exponentially as the number of nucleons increases. Current computational resources limit the direct diagonalization of the Hamiltonian matrix using the Lanczos algorithm to M-scheme basis spaces (total angular momentum projection is fixed in the basis) with a

dimension of around 10^{10} as indicated in figure 1 (left). In order to access heavier nuclei beyond the p-shell region with larger basis dimensions, many efforts have been devoted to the NCSM calculations. One of these approaches is the Importance-Truncated NCSM [4] where the model spaces are extended by using an importance measure evaluated with perturbation theory. Another approach is the Symmetry-Adapted NCSM [5] where the model spaces are truncated by the selected symmetry groups. Similar to these attempts, the no-core Monte Carlo Shell Model (MCSM) [6, 7, 8] is one of the promising candidates to go beyond the Full Configuration Interaction (FCI) method which is a different truncation of the basis states than the one commonly used in the NCSM. Shell-model calculations with an assumed inert core by the MCSM have succeeded in obtaining the approximated solutions where the direct diagonalization is difficult due to large dimensionalities as described in figure 1 (right).

In these proceedings, we focus on the latest application of the MCSM toward the *ab initio* no-core calculations, which has become viable recently with the aid of major developments in the MCSM algorithm [8, 9, 10] and also a remarkable growth in the computational power of state-of-the-art supercomputers. The overview of the benchmarks in the no-core MCSM is based on the results presented in [7, 8]. Moreover, we compare the radial density of the ^{4}He 0^+ ground state from the MCSM and FCI methods. An initial attempt to draw the intrinsic density from no-core MCSM wave functions can be found in [8].

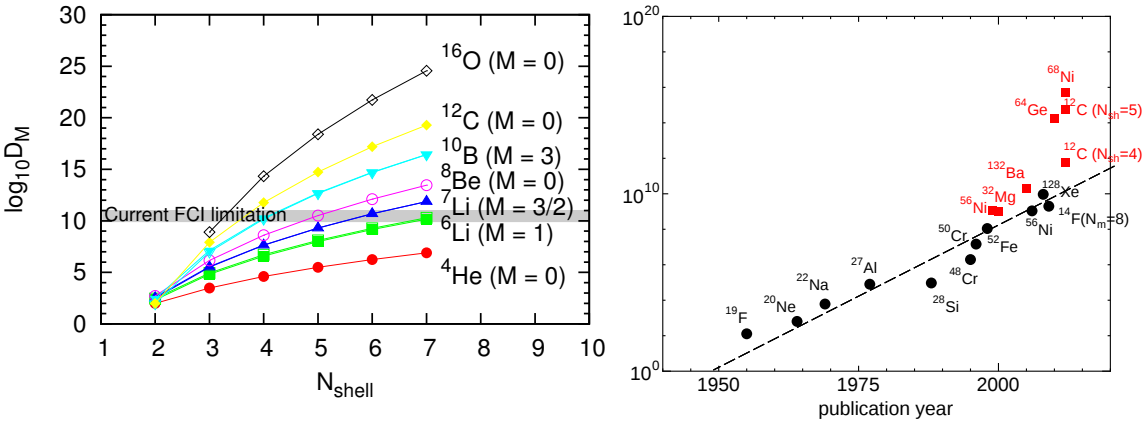

Figure 1. M-scheme dimension for light nuclei as a function of basis space cutoff, $N_{\rm shell}$ (left) and M-scheme dimension for conventional shell-model calculations with an assumed inert core as a function of publication year (right). Red squares are for the MCSM results, and black circles are for the conventional shell-model results by the direct diagonalization with the Lanczos technique.

2. MCSM

The MCSM has been developed mainly for conventional shell-model calculations with an assumed inert core [11]. Recently the algorithm and code itself have been heavily revised and rewritten so as to accommodate massively parallel computing environments [8, 9, 10]. In this section, we briefly overview the MCSM and introduce some of recent developments. An initial attempt for the application on K computer is also presented shortly.

2.1. Brief overview

The MCSM approach [11] proceeds through a sequence of diagonalization steps within the Hilbert subspace spanned by the deformed Slater determinants in the harmonic oscillator (HO) single-particle basis as the selected importance-truncated bases. Here in this subsection, we

describe our many-body wave function and Hamiltonian adopted. Some technical details and equations needed for the discussion in the following subsections are also presented shortly. See regular and review articles [8, 9, 10, 11] for a detailed account.

2.1.1. Many-body wave function A many-body basis state $|\Psi^{J^\pi M}\rangle$ is approximated as a linear combination of non-orthogonal angular-momentum (J) and parity (π) projected deformed Slater determinants with good total angular momentum projection (M),

$$|\Psi^{J^\pi M}\rangle = \sum_{n=1}^{N_b} f_n \sum_{K=-J}^{J} g_{nK} P^J_{MK} P^\pi |\phi_n\rangle, \tag{1}$$

where N_b is the number of the Slater determinants selected stochastically. P^J_{MK} is the projection operator for the total angular momentum J with its z-projection in the laboratory (body-fixed) frame, M (K). P^π is the projection operator for the parity.

In the actual computations, the integrations for the angular-momentum and parity projections are performed in parallel by discretizing the integrals on discrete mesh points. The angular-momentum projection operator is discretized as

$$P^J_{MK} = \frac{2J+1}{8\pi^2} \int d\Omega {D^J_{MK}}^* R(\Omega) \to \sum_{\lambda}^{N_\lambda} W^{J(\lambda)}_{MK} R^{(\lambda)}, \tag{2}$$

with the Euler angles, $\Omega \equiv (\alpha, \beta, \gamma)$, and the Wigner D matrix, D^J_{MK}. $R(\Omega)$ is the rotation operator, $R(\alpha, \beta, \gamma) \equiv e^{i\alpha J_z} e^{i\beta J_y} e^{i\gamma J_z}$. N_λ is the number of mesh points for discretized Euler angles. In the discretized summation over λ,

$$W^{J(\lambda)}_{MK} = \frac{1}{N_\lambda} \frac{2J+1}{8\pi^2} {D^J_{MK}}^*(\alpha_\lambda, \beta_\lambda, \gamma_\lambda), \tag{3}$$

is the weight for the sum and $R^{(\lambda)} = R(\alpha_\lambda, \beta_\lambda, \gamma_\lambda)$ is the rotational operator at the Euler angle $\Omega_\lambda = (\alpha_\lambda, \beta_\lambda, \gamma_\lambda)$. The parity projection operator is written as

$$P^\pi = \frac{1 + \pi\Pi}{2} = \sum_{\nu=1,2} W^{\pi(\nu)} \Pi^{(\nu)}, \tag{4}$$

with the parity transformation, Π, and the weight for positive and negative parity,

$$W^{\pi(\nu)} = \pi^{(\nu)}. \tag{5}$$

Note that $\pi^{(1)} = 1/2$, $\pi^{(2)} = \pi/2$, $\Pi^{(1)} = 1$, and $\Pi^{(2)} = \Pi$.

The deformed Slater determinant in (1) is described as

$$|\phi\rangle = \prod_{i=1}^{A} a_i^\dagger |-\rangle, \tag{6}$$

with the vacuum $|-\rangle$ and the creation operator,

$$a_i^\dagger = \sum_{\alpha=1}^{N_{\rm sp}} c_\alpha^\dagger D_{\alpha i}. \tag{7}$$

$N_{\rm sp}$ is specified by the cutoff of the single particle basis space, $N_{\rm shell}$. The transformation coefficients $D_{\alpha i}$ form the complex $N_{\rm sp} \times A$ matrix with the normalization condition, $D^\dagger D = 1$.

2.1.2. Hamiltonian In usual *ab initio* shell-model calculations, the intrinsic Hamiltonian is expressed as

$$H = T_{\rm rel} + V_{\rm NN} + V_{\rm 3N} + \cdots + V_{\rm Coulomb}, \tag{8}$$

where $T_{\rm rel}$ is the relative kinetic energy. The $V_{\rm NN}$ and $V_{\rm 3N}$ represent two- and three-nucleon interactions, respectively. The $V_{\rm Coulomb}$ denotes the Coulomb interaction. As explicit three-nucleon forces have not yet been treated in the MCSM algorithm, the Hamiltonian considered in this work consists of one- and two-body interactions only,

$$\begin{aligned} H &= H^{(1)} + H^{(2)} = T_{\rm rel} + V_{\rm NN} \\ &= \sum_{ij} t_{ij} c_i^\dagger c_j + \frac{1}{2} \sum_{ijkl} v_{ijkl} c_i^\dagger c_j^\dagger c_l c_k, \end{aligned} \tag{9}$$

where $H^{(1)}$ and $H^{(2)}$ are one- and two-body terms. $c_i^\dagger$ and c_i are the creation and annihilation operators of single-particle state i, respectively. Here, the Coulomb interaction is also omitted in this study.

In order to obtain eigenvalues and eigenfunctions, the coefficients, f_n and g_{nK}, in (1) are determined by solving the generalized eigenvalue problem,

$$\sum_{nK} \mathcal{H}_{mM,nK} f_n g_{nK} = \mathcal{E} \sum_{nK} \mathcal{N}_{mM,nK} f_n g_{nK}, \tag{10}$$

with the normalization condition, $\langle \Psi^{J^\pi M} | \Psi^{J^\pi M} \rangle = 1$, so that $\sum_n f_n^* f_n = 1$ and $\sum_K g_{nK}^* g_{nK} = 1$. $\mathcal{N}_{mM,nK}$ and $\mathcal{H}_{mM,nK}$ are the norm and Hamiltonian matrix spanned by the deformed Slater determinants,(6), respectively.

From (2) and (4), the norm matrix can be expressed as

$$\mathcal{N}_{mM,nK} = \langle \phi_m | P^J_{MK} P^\pi | \phi_n \rangle \to \sum_{\lambda\nu} W^{J(\lambda)}_{MK} W^{\pi(\nu)} \langle \phi_m | \phi_n^{(\lambda\nu)} \rangle, \tag{11}$$

with

$$\langle \phi_m | \phi_n^{(\lambda\nu)} \rangle = \det \left(D^{m\dagger} D^{n(\lambda\nu)} \right). \tag{12}$$

Note that $|\phi_n^{(\lambda\nu)}\rangle = R^{(\lambda)} \Pi^{(\nu)} |\phi_n\rangle$ and the matrix D^n characterizes the n-th single Slater determinant $|\phi_n\rangle$ as in (7).

The Hamiltonian matrix can be also written as

$$\begin{aligned} \mathcal{H}_{mM,nK} &= \langle \phi_m | H P^J_{MK} P^\pi | \phi_n \rangle \\ &\to \sum_{\lambda\nu} W^{J(\lambda)}_{MK} W^{\pi(\nu)} \langle \phi_m | H R^{(\lambda)} \Pi^{(\nu)} | \phi_n^{(\lambda\nu)} \rangle \\ &= \sum_{\lambda\nu} W^{J(\lambda)}_{MK} W^{\pi(\nu)} \langle \phi_m | \phi_n^{(\lambda\nu)} \rangle {\rm Tr} \left(\rho^{(\lambda\nu)} \left(t + \frac{1}{2} \Gamma^{(\lambda\nu)} \right) \right), \end{aligned} \tag{13}$$

where the generalized density matrix, $\rho^{(\lambda\nu)}$, and the self-consistent field, $\Gamma^{(\lambda\nu)}$, are defined, respectively, as

$$\rho^{(\lambda\nu)}_{ij} = \frac{\langle \phi_m | c_j^\dagger c_i | \phi_n^{(\lambda\nu)} \rangle}{\langle \phi_m | \phi_n^{(\lambda\nu)} \rangle} = \left(D^{n(\lambda\nu)} \left(D^{m\dagger} D^{n(\lambda\nu)} \right)^{-1} D^{m\dagger} \right)_{ij}, \tag{14}$$

$$\Gamma^{(\lambda\nu)}_{ik} = \sum_{jl} \bar{v}_{ijkl} \rho^{(\lambda\nu)}_{lj}, \tag{15}$$

with the antisymmetrized two-body matrix element (TBME), $\bar{v}_{ijkl} = v_{ijkl} - v_{ijlk}$. The most-time consuming part in the MCSM is the computation of $\Gamma^{(\lambda\nu)}_{ik}$. Recent improvement for the computation related to the TBMEs is discussed in section 2.2.1.

2.1.3. Basis search First, we stochastically sample the coefficients $D_{\alpha i}$ in (7) among all possible many-body basis states around the mean field solutions through the auxiliary fields $\vec{\sigma}$ with the aid of the imaginary-time evolution of the state vector,

$$|\phi(\vec{\sigma})\rangle \propto e^{-\Delta\beta h(\vec{\sigma})}|\phi^{(0)}\rangle, \tag{16}$$

where $\Delta\beta$ is the time slice of the evolution and h is the one-body Hamiltonian derived by using the Hubbard-Stratonovich transformation [11]. We then diagonalize the Hamiltonian matrix within the subspace spanned by these N_b bases, and obtain the coefficients f_n and g_{nK} in (1). Stochastically sampled bases are accepted so as to minimize the energy variationally. Therefore the MCSM can evade the so-called negative sign problem, which is the fundamental issue that cannot be avoided in quantum Monte Carlo methods. With increasing MCSM basis dimension, N_b, the ground state energy of a MCSM calculation converges from above to the exact value. The energy, therefore, always gives the variational upper bound in this framework. Recently, in the step of the basis search, we adopt the conjugate gradient (CG) method by using D as a gradient vector for minimizing the energy in addition to the initial basis search with a stochastic sampling of D through $\vec{\sigma}$ [8, 10]. The CG process gives the reduction of the number of basis states around 30% to obtain the same level of accuracy in the existing code which generates candidates of the Slater determinant only by the stochastic sampling.

An exploratory no-core MCSM investigation demonstrating a proof-of-principle has been performed for the low-lying states of the beryllium isotopes by applying the existing MCSM algorithm without introducing the recent developments [6]. Recent improvements on the MCSM algorithm have enabled significantly larger calculations [8, 9, 10]. We adopt these improvements in the present work [7, 8].

2.2. Recent developments

Among the recently achieved developments of our MCSM algorithm [8, 9, 10], in this subsection, we focus on two improvements; (1) the efficient computation of the TBMEs for the most time-consuming part in our calculations [8, 9] and (2) the energy-variance extrapolation for our MCSM (approximated) results to the FCI (exact) ones [8, 10]. There are other improvements, such as the CG method in the process of the basis search and the reordering technique in the energy-variance extrapolations. We refer for the details of these improvements to [8, 10].

2.2.1. Efficient computation of the TBMEs One of the main issues in the shell-model calculations is to evaluate TBMEs efficiently. As the matrix for the TBMEs is sparse in general, the indirect-index (list-vector) method is usually adopted by storing only the values of the non-zero matrix element and their indices. The indirect-index method is also known as the coordinate format (COO) in computer science, which is one of the most flexible and simplest formats for the sparse matrix representation. However, it tends to give slow performance due to the irregular memory access patterns.

Alternatively, in our recent MCSM code, we transform the sparse matrix to a block matrix with dense blocks by utilizing the symmetries of the two-body interaction [9]. The one-body density-matrix elements ρ_{ij} are grouped as $\tilde{\rho}(\Delta m)$ according to $\Delta m \equiv j_z(j) - j_z(i)$ where i and j are the labels for the state. The TBMEs, $\bar{v}$'s, are also similarly categorized into $\tilde{v}$. Then, the two-body part of the Hamiltonian overlap can be expressed as

$$\sum_{ik}^{N_s} \rho_{ki}\,\Gamma_{ik}^{(\lambda\nu)} = \sum_{ijkl}^{N_s} \rho_{ki}\,\bar{v}_{ijkl}\,\rho_{lj}^{(\lambda\nu)} = \sum_{\Delta m}\sum_{\alpha\beta} \tilde{\rho}(-\Delta m)_\alpha \tilde{v}(-\Delta m, \Delta m)_{\alpha\beta} \tilde{\rho}^{(\lambda\nu)}(\Delta m)_\beta, \tag{17}$$

where the last equality is derived from the necessary condition for $\tilde{v}_{ijkl}$ being non-zero: $j_z(i) + j_z(j) = j_z(k) + j_z(l)$, i.e., $\Delta m \equiv j_z(k) - j_z(i) = -(j_z(l) - j_z(j))$. N_s represents

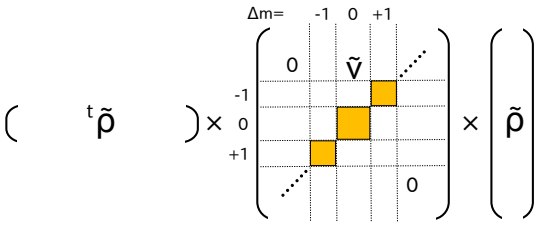

Figure 2. Schematic illustration of the (vector)^t × (matrix) × (vector) operation.

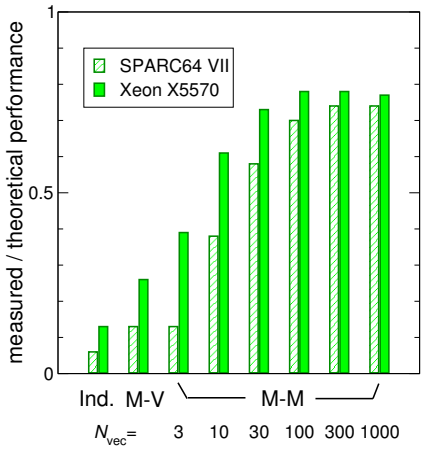

Figure 3. Comparison of the computational performance among the indirect-index method (Ind.), matrix-vector method (M-V) and matrix-matrix method (M-M) with different $N_{\rm vec}$ measured on the SPARC64 VII and Xeon X5570 systems. The values are normalized by their theoretical peak performance. See [9] for the details.

the single-particle state in a given model space. Note that $\bar{v}$ is the antisymmetrized TBME. Figure 2 is the schematic illustration of the (vector)^t × (matrix) × (vector) operation expressed with (17), (matrix) × (vector). As seen in figure 2, the sparse matrix $\bar{v}$ is transformed to a block-antidiagonal matrix $\tilde{v}$ whose blocks are dense submatrices.

Furthermore, most of the computational time is devoted to the (matrix) × (vector) operation. It is usually repeated a number of times for different vectors, $\tilde{\rho}^{(\lambda\nu)}$ with the same matrix, $\tilde{v}$. By binding $N_{\rm vec}$ $\tilde{\rho}^{(\lambda\nu)}$-vectors into a matrix, $\theta^{(\lambda\nu)}$, repeated (matrix)×(vector) operations are replaced by a (matrix) × (matrix) operation at once,

$$(\tilde{\Gamma}_1^{(\lambda\nu)}, \tilde{\Gamma}_2^{(\lambda\nu)}, \ldots, \tilde{\Gamma}_{N_{\rm vec}}^{(\lambda\nu)}) = (\tilde{v}\tilde{\rho}_1^{(\lambda\nu)}, \tilde{v}\tilde{\rho}_2^{(\lambda\nu)}, \ldots, \tilde{v}\tilde{\rho}_{N_{\rm vec}}^{(\lambda\nu)}) \equiv \tilde{v}\theta^{(\lambda\nu)}, \tag{18}$$

where the number of columns $N_{\rm vec}$ can be chosen arbitrarily. As shown in figure 3, this matrix product is computed with the BLAS level 3 library and we can achieve $70-80\%$ of the peak performance with $N_{\rm vec} \sim 30-100$ in the test case of the (matrix) × (matrix) operation [9].

2.2.2. Energy-variance extrapolation to the FCI results With increasing Monte Carlo basis dimension N_b, the MCSM results converge to the FCI results from above. In order to estimate the exact FCI answer, we extrapolate the energy and other observables evaluated by MCSM wave functions using the energy variance [8, 10]. That is, the MCSM results are plotted as a

function of the evaluated energy variance,

$$\Delta E_2 = \langle\Psi|H^2|\Psi\rangle - (\langle\Psi|H|\Psi\rangle)^2 \tag{19}$$

and then extrapolated to zero variance.

This kind of extrapolation has been enabled recently by the growth of the computational power and the factorization of the formula. In order to evaluate the expectation value of H^2, we have to compute

$$\langle\Psi^{J^\pi M}|H^2|\Psi^{J^\pi M}\rangle = \sum_{m,M,n,K,\lambda,\nu} f^*_m g^*_{mM} f_n g_{nK} W^{J(\lambda)}_{MK} W^{\pi(\nu)} \langle\phi_m|H^2|\phi^{(\lambda\nu)}_n\rangle. \tag{20}$$

The obstacle in the implementation was the large amount of computation to evaluate $\langle\phi_m|H^2|\phi^{(\lambda\nu)}_n\rangle$. Suppose H^2 is a general four-body operator, the evaluation of the matrix element involves the eightfold-loop summation of the 24 terms of products of four generalized one-body density matrices, ρ. However, due to the separability of H^2, the evaluation of the matrix element can be factorized as

$$\begin{aligned}\frac{\langle\phi_m|H^2|\phi^{(\lambda\nu)}_n\rangle}{\langle\phi_m|\phi^{(\lambda\nu)}_n\rangle} &= \sum_{i<j,\alpha<\beta}\left\{\sum_{k<l}\bar{v}_{ijkl}\left[(1-\rho^{(\lambda\nu)})_{k\alpha}(1-\rho^{(\lambda\nu)})_{l\beta} - (1-\rho^{(\lambda\nu)})_{l\alpha}(1-\rho^{(\lambda\nu)})_{k\beta}\right]\right\} \\ &\times\left\{\sum_{\gamma<\delta}\bar{v}_{\alpha\beta\gamma\delta}(\rho^{(\lambda\nu)}_{\gamma i}\rho^{(\lambda\nu)}_{\delta j} - \rho^{(\lambda\nu)}_{\delta i}\rho^{(\lambda\nu)}_{\gamma j})\right\} \\ &+\mathrm{Tr}\left[(t+\Gamma^{(\lambda\nu)})(1-\rho^{(\lambda\nu)})(t+\Gamma^{(\lambda\nu)})\rho^{(\lambda\nu)}\right] \\ &+\left\{\mathrm{Tr}\left[\rho^{(\lambda\nu)}\left(t+\frac{1}{2}\Gamma^{(\lambda\nu)}\right)\right]\right\}^2.\end{aligned} \tag{21}$$

Here, the trivial summations and their indices for the matrix products are omitted for readability. This factorization reduces the eightfold loop into a sixfold loop and decreases the computation time drastically. Note that the similar transformation to block matrices discussed in section 2.2.1 is also utilized in the evaluation of (21) so that the computation time is further reduced.

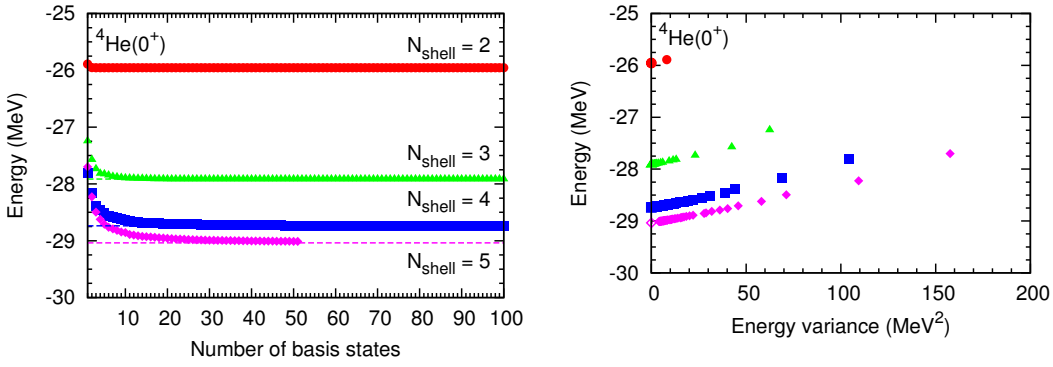

Figure 4. ^{4}He ground-state energies as functions of number of basis states (left) and energy variance (right). From the above to the bottom, the symbols (horizontal dashed lines in the left figure and open symbols at the zero energy variance in the right figure) are the MCSM (FCI) results in $N_{shell} = 2$, 3, 4 and 5, respectively. See [7] for the details.

As a typical example of the implementation, the behavior of the ground-state energies of ^{4}He (0^+) with respect to the number of basis states and to the energy variance are shown in figure 4.

From figure 4, one can see that the MCSM results can be extrapolated into the FCI ones by using the quadratic fit function of $E(\Delta E_2) = E(\Delta E_2 = 0) + c_1 \Delta E_2 + c_2 (\Delta E_2)^2$ with the fit parameters, $E(\Delta E_2 = 0)$, c_1, and c_2.

2.3. Test runs on K computer

At the initial stage of the implementation of K computer, we have performed some test calculations to measure our code performance. In this subsection, we show some of the test calculations: the ratio to the peak performance and the parallel efficiency of our code.

2.3.1. Ratio to the peak performance In order to measure our code performance on K computer, we have chosen the optimization of 15th basis dimension of the wave function in $N_{\rm shell} = 5$ with 100 CG iterations without the preprocessing as a test case. The code has run on K computer by using MPI/OpenMP with 8 threads.

Figure 5 illustrate our recent MCSM code performance. The left panel of figure 5 shows the ratio to the peak performance in the calculation of the ^{4}He 0^+ ground state. Although the performance decreases as the number of CPU cores increases, it is around 30 - 40% up to 30720 cores (8 cores per node). The right panel of figure 5 shows the ratio to the peak performance as a function of the atomic numbers. The nuclear states listed in the figure are for the ground state of each nucleus. From the figure, the dependence of the performance on atomic number A is relatively weak for the number of nucleons at least up to $A = 12$.

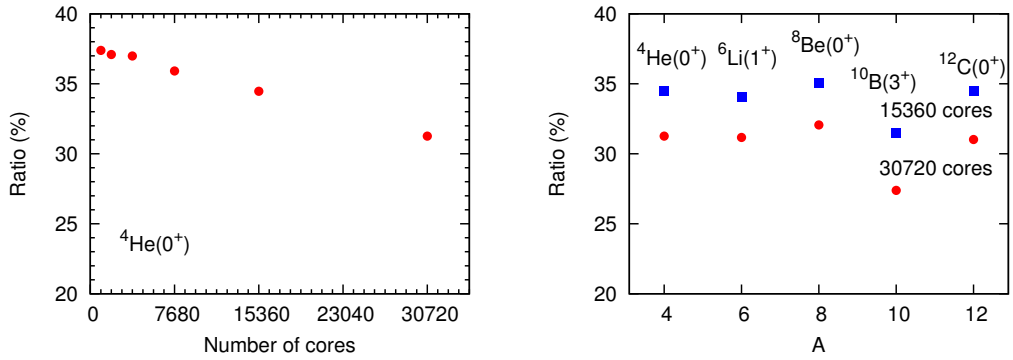

Figure 5. Ratio to the peak performance of the MCSM test calculations. Peak ratio of the calculation for the ^{4}He (0^+) ground state as a function of the number of cores (left). Peak ratio of the calculation for the ground states as a function of the number of nucleons (right). Red circles denotes the results with 30720 cores, and blue squares are with 15360 cores.

2.3.2. Parallel efficiency For testing the parallel efficiency, we have measured the dependence on the number of CPU cores. Figure 6 demonstrates the speedup (left) and the strong scaling (right) of our MCSM code on K computer as a function of the cores. The test case is the optimization of the 15th (48th) basis for ^{4}He 0^+ ground state in $N_{\rm shell} = 5$ (6) with 100 CG iterations without the preprocessing. Each setup has been chosen so that the number of MPI tasks is divisible by $N_{\rm procs}$, for simplicity. $32 \times 32 \times 30$ mesh points are used for the angular momentum projection, and 2 for the parity projection.

The left panel describes the speedup with arbitrary unit. In figure 6, the dotted line describes the perfect (ideal) scaling. The right panel of figure 6 is about the strong scaling. Here $\alpha_{\rm strong}$ is defined by the ratio of the time T with the number of CPU cores $N_{\rm procs}$ as $\alpha_{\rm strong} \equiv T(N_{\rm procs})/(T(N_{\rm procs}/2) \times 2)$. In this definition, $\alpha_{\rm strong} = 1$ describes the perfect strong

scaling. As seen in figure 6, the strong scaling is nearly perfect up to 98304 cores both in $N_{\rm shell} = 5$ and 6.

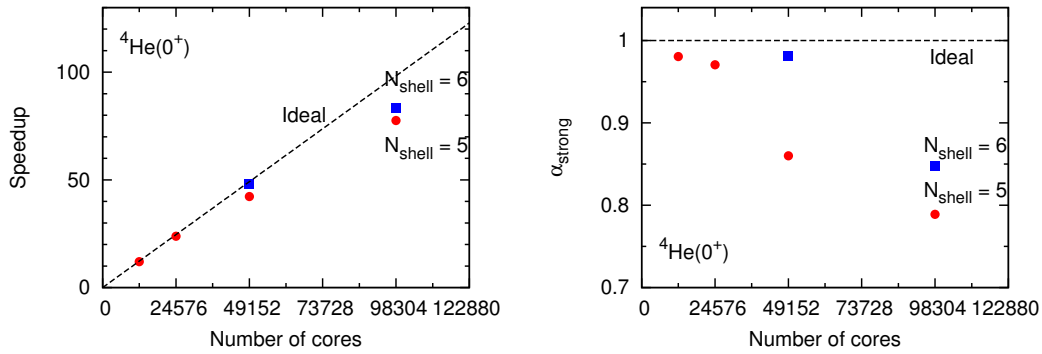

Figure 6. Speedup of the parallel computation with arbitrary unit (left), and the strong scaling (right).

3. Application

In this section, we show some of benchmark results for light nuclei. Also, the comparison of the radial density from the MCSM and FCI many-body wave functions are briefly presented in the case of ^{4}He ground state as an example.

3.1. Benchmarks

Owing to the recent development of the MCSM algorithm [8, 9, 10], we have performed the benchmark of no-core MCSM calculations [7, 8]. Figure 7 is the main outcome of the benchmark. In figure 7, we illustrate the comparisons of the energies for each state and model space between the MCSM and FCI methods. The FCI gives the exact energies in the finite model spaces, while the MCSM gives approximated ones. Thus the comparisons between them show how well the MCSM works in no-core calculations. Furthermore, we also plot the No-Core Full Configuration (NCFC) [12] results for the states of $4 \leq A \leq 10$ as the fully converged energies in the infinite model space, with assessed uncertainties visible in some cases.

For this benchmark comparison, the JISP16 two-nucleon interaction [13] is adopted and the Coulomb force is turned off. Isospin symmetry is assumed. The energies are evaluated for the optimal HO frequencies where the calculated energies are minimized for each state and model space. Here the contributions from the spurious center-of-mass (CM) motion are ignored for simplicity. The comparisons are made for the states; ^{4}He (0^+), ^{6}He (0^+), ^{6}Li (1^+), ^{7}Li ($1/2^-$, $3/2^-$), ^{8}Be (0^+), ^{10}B (1^+, 3^+) and ^{12}C (0^+). The model space ranges from $N_{shell} = 2$ to 5 for $A \leq 6$ (4 for $A \geq 7$). Note that the energies of ^{10}B (1^+, 3^+) and ^{12}C (0^+) in $N_{shell} = 4$ are available only from the MCSM results. The M-scheme dimensions for these states are already close to or above the current computational limitation in the FCI approach. The numbers of MCSM basis states are taken up to 100 in $N_{shell} = 2 - 4$ and 50 in $N_{shell} = 5$.

As seen in figure 7, the energies are consistent with each other where the FCI results are available to within ~ 100 keV (~ 500 keV) at most of the MCSM results with(out) the energy-variance extrapolation of the MCSM results. The other observables; the point-particle root-mean-square matter radii and electromagnetic moments also give reasonable agreements between the MCSM and FCI results. The detailed comparisons among the MCSM, FCI, and NCFC methods are discussed in [7].

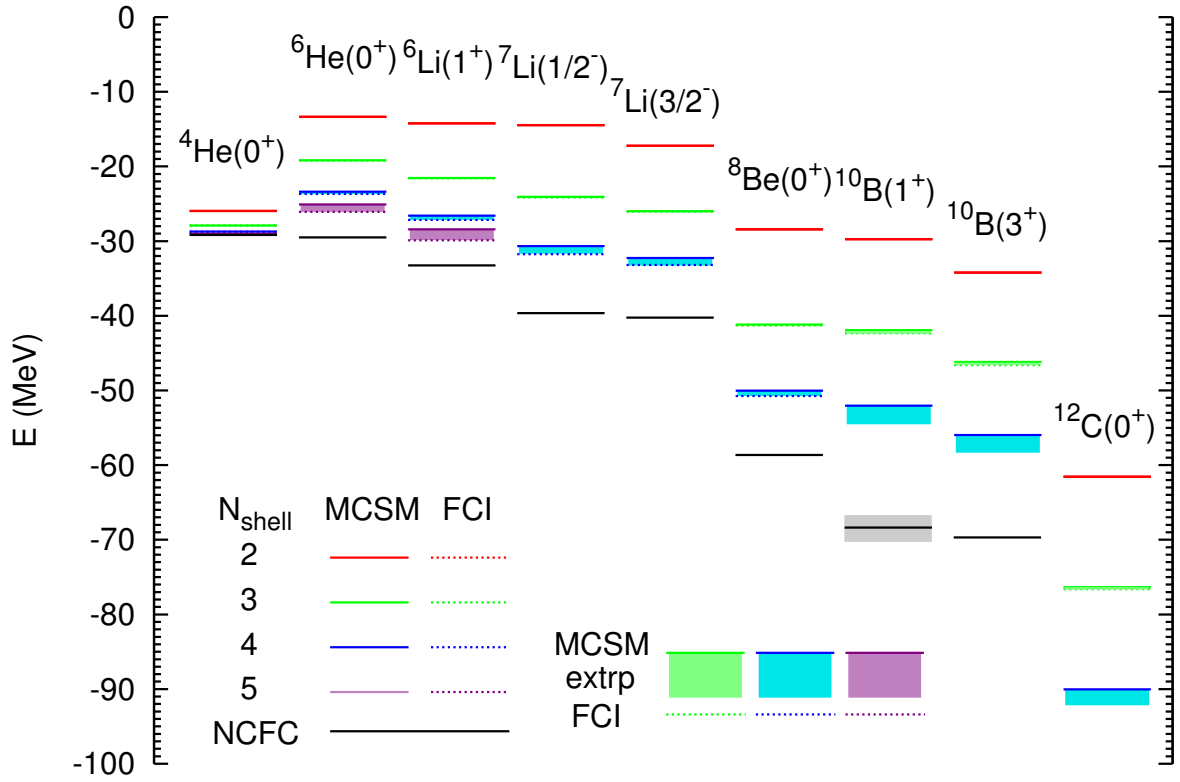

Figure 7. Comparisons of the energies between the MCSM and FCI along with the fully converged NCFC results where available. The NCFC result for the ^{10}B(1$^+$) state has a large uncertainty indicated by the grey band. The MCSM (FCI) results are shown as the solid (dashed) lines that nearly coincide where both are available. The extrapolated MCSM results are illustrated by bands. From top to bottom, the truncation of the model space is $N_{\rm shell} = 2$ (red), 3 (green), 4 (blue), and 5 (purple). Note that the MCSM results are extrapolated by the energy variance with the second-order polynomials. Also note that all of the results of ^{10}B and ^{12}C at $N_{\rm shell} = 4$ were obtained only with MCSM. Taken from [7].

3.2. Radial density of the ^{4}He ground state

The intrinsic local density is one of the basic quantities to understand the structure of nuclei intuitively. It is, however, challenging to obtain it from *ab initio* calculations. For example, the α-cluster structure of the ground and two excited states of ^{8}Be has been studied by the Variational Monte Carlo (VMC) and GFMC calculations with realistic nuclear forces [14]. They have attempted to obtain the intrinsic density in body-fixed coordinates by computing the moment of inertia matrix for each configuration and then diagonalizing them to rotate the configurations along the principal axis. Motivated by these analyses, we try to extract an intrinsic density from MCSM wave functions in a similar way adopted in the VMC and GFMC calculations [8, 15].

In shell-model calculations, we use single-particle coordinates, and the A-body wave function describes both the CM and relative motions. Using HO single-particle wave functions in combination with the $N_{\rm max}$ truncation (a truncation on the total number of HO quanta in the many-body basis), as is commonly done in the NCSM, the CM and relative wave functions factorize exactly. This allows for a deconvolution of the CM and translationally-invariant

densities using three-dimensional Fourier transformations [16]. In [17], this method is used to show α-cluster structure for the ground state of ^{9}Be. Neither in the FCI calculations nor in the MCSM, however, do we have such an exact factorization.

In the MCSM, the one-body density is computed by using the MCSM wave function, equation (1),

$$\rho(\vec{r}) = \langle \Psi^{J^\pi M} | \sum_i \delta^3(\vec{r} - \vec{r}_i) | \Psi^{J^\pi M} \rangle \tag{22}$$

with the coordinate of the i-th nucleon, $\vec{r}_i$. Integrated over the angular directions, this gives the radial density, $\rho(r) = \int d\Omega \rho(\vec{r})$. Note that this density includes the CM motion. In principle, we could obtain the translationally-invariant one-body density in relative coordinates from the two-body density in single-particle coordinates, analogous to the calculation of the intrinsic rms radius by using a two-body operator, $\hat{r}^2 = (\hat{r}_i - \hat{r}_j)^2$, whereas the naive one-body operator, $\hat{r}_i^2$, gives us the rms radius that includes the effects of the CM motion.

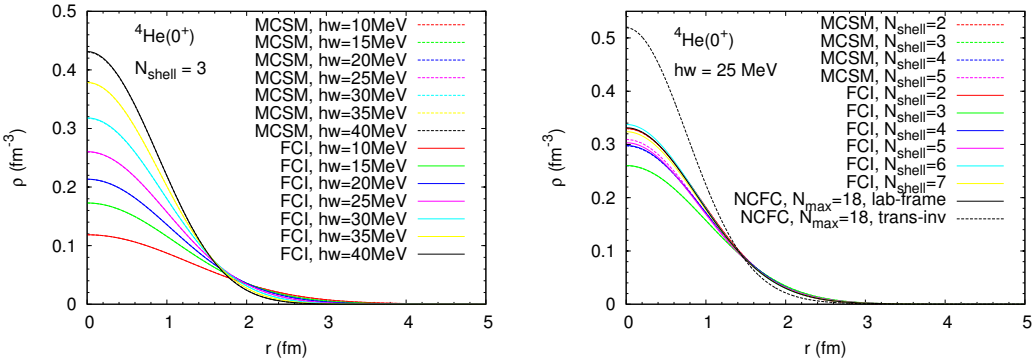

Figure 8. The radial density ρ of the ^{4}He ground state as a function of radius r for various HO energies $\hbar\omega$'s in the basis cutoff $N_{\rm shell} = 3$ (left), and for various $N_{\rm shell}$'s with $\hbar\omega = 25$ MeV (right). Both in the figures, the dashed (solid) curves denote the MCSM (FCI) results. In the left figures, the MCSM and FCI results agree well, and the differences are unrecognizable. For comparison, in the right figure, we include NCFC results before and after the deconvolution of the CM effect, corresponding to the lab-frame and translationally-invariant densities, respectively.

Figure 8 is the comparison of the radial densities of ^{4}He ground state using MCSM, and FCI, including the effects of the CM motion. The left figure shows the dependence of the radial density ρ on the HO parameter $\hbar\omega$, while the right figure is for the dependence on the basis cutoff $N_{\rm shell}$. For comparison, we also include the NCFC result in the right figure, both before and after the deconvolution of the CM motion. In the figure, these are labeled by "lab-frame" and "trans-inv", respectively. From figure 8, the MCSM and FCI results agree quite well. The small discrepancies (especially for the case of $N_{\rm shell} = 5$ in the right figure) come from the fact that MCSM results for ρ are not extrapolated to the FCI basis cutoff by using the energy variances. The left figure clearly shows that there is a strong dependence on HO parameter $\hbar\omega$. This is due to the fact not only that ρ is not converged in such a small basis space, $N_{\rm shell} = 3$, but also that the CM motion is strongly $\hbar\omega$ dependent. Even in the limit $N_{\rm shell}$ to infinity, these densities will depend strongly on $\hbar\omega$. Furthermore, the convergence with $N_{\rm shell}$ is not monotonic, as can be seen in the right figure, most likely because the CM motion is different for different $N_{\rm shell}$ values. Note that the density is comparable to the density in lab-frame coordinates obtained with the NCFC approach, suggesting that in the MCSM and FCI approaches the CM motion is approximately a $0s$ HO wave function. The translationally-invariant density, however, has a significantly larger central density, and falls off more rapidly: the effect of the CM motion is to smear out the translationally-invariant density [16].

4. Summary

By exploiting the recent development in the computation of the Hamiltonian matrix elements between non-orthogonal Slater determinants and the technique of energy-variance extrapolation, the no-core calculations with the MCSM algorithm can be performed efficiently on massively parallel supercomputers. From the benchmark calculations, the observables give good agreement between the MCSM and FCI results in the p-shell nuclei. The code performance of our MCSM on K computer was tested at the initial stage of implementation. We also present the comparison of the radial density of ^{4}He ground state among MCSM, FCI, and NCFC methods as an initial demonstration towards the intuitive description of nuclear shapes from shell-model calculations.

Acknowledgments

This work was supported in part by the SPIRE Field 5 from MEXT, Japan. We also acknowledge Grants-in-Aid for Young Scientists (Nos. 20740127 and 21740204), for Scientific Research (Nos. 20244022 and 23244049), and for Scientific Research on Innovative Areas (No. 20105003) from JSPS, and the CNS-RIKEN joint project for large-scale nuclear structure calculations. This work was also supported in part by the US DOE Grants No. DESC0008485 (SciDAC-3/NUCLEI), and DE-FG02-87ER40371, by US NSF grant 0904782, and through JUSTIPEN under grant No. DE-FG02-06ER41407. A part of the MCSM calculations was performed on the T2K Open Supercomputer at the University of Tokyo and University of Tsukuba, and the BX900 Supercomputer at JAEA. Computational resources for the FCI and NCFC calculations were provided by the National Energy Research Supercomputer Center (NERSC), which is supported by the Office of Science of the U.S. Department of Energy under Contract No. DE-AC02-05CH11231, and by the Oak Ridge Leadership Computing Facility at the Oak Ridge National Laboratory, which is supported by the Office of Science of the U.S. Department of Energy under Contract No. DE-AC05-00OR22725.

References

[1] Pieper S C, Wiringa R B and Carlson J 2004 *Phys. Rev.* C **70** 054325; Nollett K M, Pieper S C, Wiringa R B, Carlson J and Hale G M 2007 *Phys. Rev. Lett.* **99** 022502
[2] Hagen G, Hjorth-Jensen M, Jansen G R, Machleidt R and Papenbrock T 2012 *Phys. Rev. Lett.* **108** 242501; 2012 *Phys. Rev. Lett.* **109** 032502 and references therein
[3] Navrátil P, Vary J P and Barrett B R 2000 *Phys. Rev. Lett.* **84** 5728; 2000 *Phys. Rev.* C **62** 054311; Quaglioni S and Navrátil P 2008 *Phys. Rev. Lett.* **101** 092501; 2009 *Phys. Rev.* C **79** 044606; Barrett B R, Navrátil P and Vary J P 2013 *Prog. Part. Nucl. Phys.* **69** 131
[4] Roth R 2009 *Phys. Rev.* C **79** 064324; Roth R, Binder S, Vobig K, Calci A, Langhammer J and Navrátil P 2012 *Phys. Rev. Lett.* **109** 052501
[5] Dytrych T, Sviratcheva K D, Bahri C, Draayer J P and Vary J P 2007 *Phys. Rev. Lett.* **98** 162503; 2008 *J. Phys.* G. **35** 095101; Dytrych T, Sviratcheva K D, Draayer J P, Bahri C and Vary J P 2008 *J. Phys.* G. **35** 123101
[6] Liu L, Otsuka T, Shimizu N, Utsuno Y and Roth R 2012 *Phys. Rev.* C **86** 014304
[7] Abe T, Maris P, Otsuka T, Shimizu N, Utsuno Y and Vary J P 2011 *AIP Conf. Proc.* **1355** 173; 2012 *Phys. Rev.* C **86** 054301
[8] Shimizu N, Abe T, Tsunoda Y, Utsuno Y, Yoshida T, Mizusaki T, Honma M and Otsuka T 2012 *Prog. Theor. Exp. Phys.* 01A205
[9] Utsuno Y, Shimizu N, Otsuka T and Abe T 2013 *Commput. Phys. Commun.* **184** 102
[10] Shimizu N, Utsuno Y, Mizusaki T, Otsuka T, Abe T and Honma M 2010 *Phys. Rev.* C **82** 061305(R); Shimizu N, Utsuno Y, Mizusaki T, Honma M, Tsunoda Y and Otsuka T 2012 *Phys. Rev.* C **85** 054301
[11] Honma M, Mizusaki T and Otsuka T 1995 *Phys. Rev. Lett.* **75** 1284; 1996 *Phys. Rev. Lett.* **77** 3315; Otsuka T, Honma M and Mizusaki T 1998 *Phys. Rev. Lett.* **81** 1588; Otsuka T, Honma M, Mizusaki T, Shimizu N and Utsuno Y 2001 *Prog. Part. Nucl. Phys.* **47** 319
[12] Maris P, Vary J P and Shirokov A M 2009 *Phys. Rev.* C **79** 14308; Maris P, Shirokov A M and Vary J P 2010 *Phys. Rev.* C **81** 021301
[13] Shirokov A M, Vary J P, Mazur A I and Weber T A 2007 *Phys. Lett.* B **644** 33; Shirokov A M, Vary J P, Mazur A I, Zaytsev S A and Weber T A 2005 *Phys. Lett.* B **621** 96

[14] Wiringa R B, Pieper S C, Carlson J and Pandharipande V R 2000 *Phys. Rev.* C **62** 014001
[15] Yoshida T, Shimizu N, Abe T and Otsuka T contribution to the CCP2012 proceedings
[16] Cockrell C, Vary J P and Maris P 2012 *Phys. Rev.* C **86** 034325
[17] Maris P 2012 *J. Phys. Conf. Ser.* **402** 012031